JAEA-Research
2022-007
DOI:10.11484/jaea-research-2022-007

# Experimental and Numerical Study on Energy Separation in Vortex Tube with a Hollow Helical Fin (Joint Research)

Masatoshi KURETA, Yoji YAMAGATA, Ken MIYAKOSHI, Tatuya MASHII
Yoshiaki MIURA and Kazunori TAKAHASHI

Planning and Co-ordination Office
Sector of Nuclear Science Research

September 2022
Japan Atomic Energy Agency
日本原子力研究開発機構

JAEA-Rsearch

国立研究開発法人日本原子力研究開発機構　JAEA イノベーションハブ　研究成果利活用課
〒 319-1195　茨城県那珂郡東海村大字白方 2 番地 4
電話 029-282-6387, Fax 029-282-5920, E-mail:ird-support@jaea.go.jp


2-4 Shirakata, Tokai-mura, Naka-gun, Ibaraki-ken 319-1195 Japan
Tel +81-29-282-6387, Fax +81-29-282-5920, E-mail:ird-support@jaea.go.jp

JAEA-Research 2022-007

# Experimental and Numerical Study on Energy Separation in Vortex Tube with a Hollow Helical Fin (Joint Research)

Masatoshi KURETA, Yoji YAMAGATA*1, Ken MIYAKOSHI*1,
Tatuya MASHII*1, Yoshiaki MIURA*1 and Kazunori TAKAHASHI*2

Planning and Co–ordination Office, Sector of Nuclear Science Research,
Japan Atomic Energy Agency
Tokai-mura, Naka-gun, Ibaraki-ken

(Received August 8, 2022)

To enhance energy separation in a counter-current Ranque-Hilsch vortex tube, a newly designed hollow helical fin was inserted into the hot tube of the vortex tube. In this study, the effect of the fin on the energy separation was investigated using three types of the vortex tube, and then computational fluid dynamics (CFD) simulation has been conducted to understand the experimental results and discuss the flow structure in the vortex tube with the hollow helical fin. As a result, it was found from the experimental data that the fin effectively enhanced energy separation, and that the tube length could be shorten. When the inlet air pressure was 0.5 MPa, the maximum temperature difference from the inlet to the cold exit was 62.2 °C. The CFD code employing the Reynolds Stress Model (RSM) turbulence model was used to analyze the fluid dynamics in the vortex tube. As a result, it was confirmed that the temperature, velocity, and pressure distributions changed significantly at the stagnation point, and that the distributions in the tube with the fin were completely different from those without the fin. It was thought that a strong reversing helical vortex flow with small recirculating vortex structure formed between the fin end and the stagnation point on the cold exit side would enhance energy separation in the vortex tube with the hollow helical fin.

Keywords: Vortex Tube, Energy Separation, Spot Cooler, Hollow Helical Fin, CFD Simulation

---

This work has been performed in Japan Atomic Energy Agency as a joint research with YAMATOH-TEKKO and ART KAGAKU.

*1 YAMATOH-TEKKO Co., Ltd.
*2 ART KAGAKU Co., Ltd.

# 中空螺旋状フィンを有するボルテックスチューブにおける
# エネルギー分離に関する実験的および数値解析的研究
（共同研究）

日本原子力研究開発機構　原子力科学研究部門　企画調整室

呉田　昌俊、山形　洋司[*1]、宮腰　賢[*1]、増井　達也[*1]、三浦　義明[*1]、高橋　一憲[*2]

（2022 年 8 月 8 日受理）

ボルテックスチューブにおけるエネルギー分離を促進するために、新たに設計した中空螺旋状フィンを管内に挿入した。本報では、3 種類の管を用いて、フィンがエネルギー分離に及ぼす影響を実験的に調べ、次に、数値流体力学（CFD）シミュレーションを行い、実験結果と中空螺旋状フィン付き管内の流動構造との関係を研究した。実験データから、フィンがエネルギー分離を促進し、管長を短くできることがわかった。入口空気圧が 0.5MPa のとき、入口から出口までの最大温度差は 62.2℃であった。レイノルズ応力モデル（RSM）乱流モデルを組み込んだ CFD コードを用いて流体解析をした結果、フィン無とフィン有の場合とで淀み点の位置が大きく変わり、流動構造が全く異なることを確認した。中空螺旋状フィンによって、低温側フィン端と淀み点との間に小さな循環渦構造を持つ強い反転渦流が形成され、乱流運動エネルギーが大きな領域が生成されることによってエネルギー分離が促進されたと考えられる。

---

本研究は、日本原子力研究開発機構と山藤鉄工およびアート科学との共同研究に基づいて実施したものである。

原子力科学研究所：〒319-1195　茨城県那珂郡東海村大字白方 2-4

＊1　山藤鉄工株式会社

＊2　株式会社アート科学

# Contents

# 目　次

## 1. Introduction

The Ranque-Hilsch vortex tube (VT) is a simple energy separation device [1-3]. The VT is mainly used for spot cooling in industry. It is used for machining machines, high temperature parts, electronic device, molds, etc. On the contrary, the air discharged from the hot exit is used for heating adhesives, shrink wrap, or drying parts. The authors initiated a study on VTs for machining applications. The requirements from the operators were as follows: an air-operated VT capable of discharging cryogenic air with as high cold mass fraction and high mass flow rate as possible. Standard commercial VTs were tested but were not satisfactory. The standard counter-current VT has a simple hot tube (cylinder) between the inlet and the hot exit [2].

VT was invented by Ranque [4] in 1934 and became widely known by Hilsch's paper [5]. Since then, many experimental and analytical studies have been conducted as the Ranque-Hilsch vortex tube. Gao [6] described that turbulence and acoustics, which are multiple circulating flows, play a more important role in the mechanism of energy separation inside the VT. Liew et al. [7,8] inferred that compression and expansion inside the hot tube are caused by turbulent vortices, and predicted a similar process of each vortex pumping heat from the axis to the periphery, and theoretically predicted the temperature based on the pressure at the exit. Xue [9,10] summarized a detailed literature review of VT, and based on visualization of the internal flow, measured data, and exergy analysis. Xue summarized the working principle of VT. According to the work of Xue et al. [9], the explanation of Liew et al. [7,8] cannot be considered as the cause of the temperature rise.

A number of experimental studies on VT have been carried out. These studies have used many different types of tubes, including simple tubes, convergent-divergent tubes [11,12], double-circuit VTs, and multi-cascade VTs [13,14]. The working fluid also include air, nitrogen, carbon dioxide, etc. VT performance has been found to be sensitive to geometric parameters including injector shape and size [15-17], hot plugging [18], etc. A number of studies on geometric parameters have been reported. Samruaisin et al. [19] reported the effect of double vortex-chambers on the energy separation.

In order to understand the principle, flow visualization and flow measurement in a hot tube were performed by Gao [6] and Xue [10]. From the observation of the tracers in the transparent tube, they also visualized the helical motion, the main flow, and the structure of the flow called multi-circulation. Multi-circulation was also verified using velocity profiles measurement data [9,10,20].

A number of researchers have also performed numerical analysis using CFD codes. In these papers, both Reynolds-Averaged Navier-Stokes (RANS) and Large Eddy Simulation (LES) methods are used to simulate the flow from inlet to outlet of the VT. For steady-state analysis, standard $k$-ε model and the RSM model are often used [21-24]. The advantage of the RANS model is that the computational cost is relatively low. However, their results show time-averaged values. On the other hand, the transition-RSM model and LES can simulate instantaneous values. Therefore, the transition vortex motion can be simulated by the transient-RSM and LES. Secchiaroli et al [22] reported the simulation results and discussion using RANS and LES, and found that secondary vortices are generated along the pipe length [25,26].

Zhang et al. [27] and Guo et al. [28] focused on the dynamic process (oscillation) of the secondary circulation layer in the tube using the transition RSM model and comparing it with the time-averaged RSM model and experimental data. The simulations by Zhang and Guo show that the reversing flow is reliably occurring at the cold end of the VT. Furthermore, the simulation results emphasized the oscillations in the boundary layer of the central recirculation zone and showed that the fluid flow in the secondary circulation zone oscillates periodically.

The ultimate goal of this research is to provide a high-performance spot cooler for machining using VT technology. Therefore, we designed a unique hollow inclined helical fin that was fixed inside the hot tube. The shape of the fins resembles a screw. However, unlike screws, it is hollow without a mandrel. In addition, it is not a screw-type vortex generator installed at the entrance [4,16]. So far, no VT with the same shape has been reported.

In this study, an experimental study was conducted to evaluate the effect of the fin on energy separation and surface temperature distribution in comparison with a standard finless VT. In addition, 3D CFD simulations using the RSM turbulence model were performed to understand the flow structure in the new VT.

## 2. Experimental study

### *2.1. Experimental setup*

The working fluid is air. The air is discharged from a screw-type oil-less compressor, stored in a tank, and then supplied to a vortex tube. This compressor is commonly used in machine shops, and its automatic control function allows the discharge pressure to fluctuate slightly at high pressure.

Fig. 1 shows a schematic diagram and photographs of the experimental setup. The inlet pressure was adjusted with a pressure regulator. All temperatures were measured using high-precision thermocouples (T-type, Class 1: error = ±0.5 °C). Mass flow rates were measured at the inlet, the cold and hot exits using the mass flow meter. The flow meters connected to the cold and hot exit pipes were opened to atmospheric pressure at their outlet ends. The cold mass fraction was adjusted by a cold mass fraction control valve connected to the hot exit of the VT. Here, the cold mass fraction $\xi = F_c/F_{in}$, where $F_c$ is a mass flow rate of air existing through the cold exit, $F_{in}$ is a mass flow rate of air at the inlet to the VT. Three types of VTs were tested, as shown in Fig. 1.; (1) a simple vortex tube (referred to as Finless in this paper), (2) a tube with a hollow helical fin (referred to as Type-A Fin), and (3) a tube with a hollow helical fin (referred to as Type-B Fin). As shown in the picture, there are six nozzles in the swirl generator. The nozzle gap (referred to as *Gap*) was 1.5 mm or 0.5 mm. Also, the height of the nozzles was uniform at 7.5 mm. The inner length $L$ of the vortex tube was 772 mm, and the inner diameter $D$ was 30.7 mm (JIS G 3459 SUS304TP 1BxSch5S), $L/D$=25.1. It was a typical length to diameter ratio of 20 – 50 for Finless VTs. The length of the hollow helical fin $L_{fin}$ of Type-A Fin and Type-B Fin was 620 mm. Fin part of the Type-A Fin and Type-B Fin were placed at the position of the heat tube of Finless shown in the figure. The Type-A Fin has a structure in which the air flows through the fin toward the periphery, and the Type-B Fin has a reversal of the Type-A Fin in which the air flows through the fin toward the central axis. No insulation is wrapped around the VT in order to record the surface temperature distribution with an infrared (IR) camera. All the system data were recorded by the data logger, monitor cameras and the IR camera. And all data were processed to HTML report files using R markdown technique on the PC.

### *2.2. Experimental conditions and results*

Fig. 2 shows the time variation of the cold air exit temperature for about 3 minutes after the inlet pressure regulator was fully opened and the air started flowing. The cold exit temperature stabilized at a steady value after one minute. In this paper, the transition data during start-up was not used, only the stable data was used. When the cold exit temperature was measured to be -45 °C in the experiment, water was sprayed on the pipe connected to the cold exit. Then, the water froze as shown in the picture.

#### *2.2.1. Effect of the nozzle gap on energy separation*

Fig. 3 shows the effect of the nozzle gap on the temperature differences. The temperature differences are defined as the differences in air temperature between the inlet and the hot exit, $\Delta T_h$, or between the inlet and the cold exit, $\Delta T_c$. Since the VT is generally used with the inlet valve fully open, in this experiment the pressure regulator was fully open as in general use. Then, only the cold mass fraction control valve was controlled to close in stages from fully open to fully closed. As shown in Fig. 3, the temperature difference at *Gap*=0.5 mm is slightly larger than that at *Gap*=1.5 mm, which is considered to be due to the larger swirl velocity at *Gap*=0.5 mm by narrowing the nozzle gap.

For a spot cooler for machining, a higher flow rate is desired. Comparing the discharge mass flow rates of *Gap*=0.5 mm VT and *Gap*=1.5 mm VT at the same inlet pressure and cold mass fraction, the *Gap*=0.5 mm VT flowed only about 0.8 times as much as the *Gap*=1.5 mm VT. Therefore, the experiment was then conducted mainly with the *Gap*=1.5 mm one, which has a higher flow rate.

### *2.2.2. Effect of the pitch and inner diameter of the hollow helical fin on energy separation*

The fabrication parameters for a hollow helical fin are the pitch of the fin and the diameter $\Phi$, which is the boundary between the hollow and fin sections. So, the combinations of fin pitch and $\Phi$ are (20 mm, 5 mm), (20 mm, 10 mm), (30 mm, 10 mm) were produced, and experiments were conducted to compare which combination could generate the largest temperature difference.

Fig. 4 shows the results of measuring the hot and cold exit temperature differences of three types of VTs with different fin pitch and $\Phi$, with *Gap* = 1.5 mm and $P_{\mathrm{in}}$ = 0.4 MPa. It was found from Fig. 4 that the temperature difference can be larger for a fin pitch of 30 mm than for 20 mm and for a $\Phi$ of 10 mm than for 5 mm.

Thereafter, the fin pitch of 30 mm and the $\Phi$ of 10 mm were set as the default for VTs to be produced. Hereafter, the results with the fin pitch of 30 mm and the $\Phi$ of 10 mm will be shown and the mention of the default will be omitted.

### *2.2.3. Effect of the hollow helical fin on energy separation*

The effect of the hollow helical fin on the temperature differences at $P_{\mathrm{in}}$ = 0.45 MPa is shown in Fig. 5. Nozzle gap, *Gap,* of the swirl generator was 1.5 mm. Here, "Type-A Fin ($D$ = 28.4 mm)" shows the modified version of Type-A Fin. The inner diameter of the hot tube was 28.4 mm (JIS G 3459 SUS304TP 1BxSch10S), not 30.7 mm (Sch5S). The maximum temperature difference $\Delta T_{\mathrm{c}}$ from inlet to cold exit was 62.2 °C when the cold mass fraction control valve was not connected to the Type-A Fin ($D$ = 28.4 mm). At that time, $\xi$ = 0.027. The temperature difference $\Delta T_{\mathrm{c}}$ of Type-A Fin was found to be 10 °C larger than that of Finless at $\xi$ = 0.35. When the cold mass fraction $\xi$ was above 0.4, the temperature difference $\Delta T_{\mathrm{c}}$ was smaller for Type-B Fin. Also, when the cold mass fraction $\xi$ was above 0.7, the temperature difference $\Delta T_{\mathrm{c}}$ was smaller for the Type-A Fin. These are considered to be due to the change in the turbulent structure in the hot tube of Type-A Fin and Type-B Fin. Since Type-A Fin is superior to Type-B Fin for general spot cooling applications, the following experiments were conducted with Type-A Fin.

The experimental data indicate that the hollow helical fin enhances energy separation.

### *2.2.4. Effect of the pressure on energy separation*

Fig. 6 shows the effect of inlet pressure on temperature differences for the Type-A Fin. The lowest cold exit temperature was measured when the cold mass fraction control valve was fully open. The highest hot exit temperature was measured when the cold mass fraction was 0.75. It was confirmed that the temperature difference $\Delta T_c$ increased with pressure.

The tendency for the temperature difference to increase with pressure was the same as the results for the Finless and also Type-A Fin *Gap*=0.5 mm.

### *2.2.5. Surface temperature distribution*

Since the surface temperature of the hot tube of the VT increases during operation, the surface temperature distribution was visualized using IR cameras. The radiant temperature was corrected using the emissivity of stainless steel and the distance between the IR camera and the VT. However, we believe that the measurement accuracy of the temperature of the condensed piping is poor.

The surface temperature distributions of the Type-A Fin recorded by the IR still camera and the corresponding photograph are shown in Fig. 7. As shown in Fig. 7 (a1), the cold exit pipe turns white when the moisture in the ambient air condenses. In the IR image of Fig. 7 (a2), the cold exit pipe is shown in dark blue, that is, this VT can work as the spot cooler. The surface temperature distribution of the hot tube varied depending on the type of VT and the cold mass fraction.

When shooting with the IR still camera, we noticed that the temperature distribution of the hot tube varied with the cold mass fraction, so we subsequently replaced the camera with an IR video camera capable of long continuous recording.

Fig. 8 shows the surface temperature distributions taken by the IR video camera. In the experiment, the cold mass fraction was varied and recorded as a movie. From Fig. 8 (a1) and (a2), it can be seen in case of the Finless that the temperature at the hot end is higher when the cold mass fraction is lower, however, the temperature at the cold side is higher when the cold mass fraction is higher. This means that the maximum surface temperature position of the Finless varies with the cold mass fraction. On the other hand, in the case of the Type A Fin shown in Fig. 8 (b1) and (b2), the temperature at the position labeled "High" in the figure was always the highest. The highest surface temperature was observed under the condition of cold mass fraction of about 0.75, as shown in Fig. 8 (b2). As shown in Fig. 5 and Fig. 6, the hot exit temperature of Type-A Fin had the maximum value when the cold mass fraction was 0.75. It was confirmed that when the surface temperature reached its maximum value, the air temperature discharged from the hot exit also reached its maximum value.

We checked the surface temperature distribution by touching the surface of the hot tube directly with our hands while the VT was in operation. It should be noted that the results of the touch and the visualization of the temperature distribution by the IR camera were in good agreement, although the temperature was too high to be grasped by hand.

## 3. Investigation with the CFD analysis

The objective of this investigation with the CFD analysis is to understand the flow characteristics in the VT with the hollow helical fin.

### *3.1. Simulation code and modeling*

The relationship between the flow characteristics and the temperature distribution in the VT was simulated by the 3D CFD code, Ansys FLUENT 2019-2020R1. The input 3D models of the VT were created from 3D CAD data which were also used to produce the actual VTs used in the experiment. It was set for analysis in which a compressible fluid flows in the flow path. First, the RANS standard $k$-ε model was selected to find the appropriate mesh generation and analysis conditions that would not cause numerical divergence. As shown in Appendix 1 - 4, the mesh was set so that the size of the part where the speed is high and the amount of change is likely to be large is small. The creation of this mesh was decided by repeating trial and error many times so as not to diverge. The number of iterations of the numerical analysis was 20,000, which was confirmed to be sufficiently convergent. Compared with the RSM model, which will be described later, the standard $k$-ε model has an analysis result in which the amount of change is small, with no particular pressure, velocity, or temperature gradient in the radial direction. Baghdad et al. [23] compared the results of numerical analysis using four different RANS models (standard $k$-ε, $k$-ω, SST $k$-ω and RSM model) with the finless experimental data. As a result, it is reported that only the RSM model was able to correctly estimate the measured cold exit temperature. Therefore, in this report, the analysis was performed using the RSM model as shown in Appendix 5. The RSM model was a ε-based Reynolds stress model. In the RSM, linear pressure-strain model was selected. And, as a wall function, standard wall function was selected. In this analysis, the energy equation is solved. Heat flux on the wall was assumed to be 0. The inlet boundary is assumed to have a constant temperature.

The boundary conditions were set so that the values were constant. The boundary conditions were set to the conditions where $P_{in}$ = 0.5 MPa, $T_{in}$ = 22 °C, and cold mass fraction = 0.2. The inlet boundary conditions were set so that the pressure was $P_{in}$ = 0.5 MPa, as the result, inlet mass flow rate $F_{in}$ became about 290 kg/h. The cold mass fraction was adjusted by changing the cross-sectional area of the hot exit end section to simulate the cold mass fraction control valve. In the experiment, as shown in Fig. 1, pipes were connected to the cold and hot exits to measure temperature, pressure, and flow rate, and the end of the pipes was opened to atmospheric pressure. On the other hand, the difference is that in the simulation, the cold and hot exits of the VT were set to release atmospheric pressure without any piping. Therefore, the analytical results for the cold and hot exits were different from the experimental data.

### *3.2. Simulation results*

#### *3.2.1. Effect of the hollow helical fin on air streamlines*

Figs. 9 (a), (b), and (c) show the 3D view of air streamlines colored by mean total velocity (referred to as velocity) in the Finless, Type-A Fin, and Type-B Fin, respectively. In the case of the Finless, the stagnation point is on the hot exit side and a long reversing current is formed on the central axis as shown in Fig. 9 (a). On the other hand, Fig. 9 (b) and (c) indicate that the stagnation point of both Type-A Fin and Type-B Fin moves to the cold end of the hollow helical fin and the reversing current becomes shorter. From the stagnation point to the hot plug, in the case of Type-A Fin, the air swirls around the periphery along the helical fin as shown in Fig. 9 (b). The details of the hot exit side will be discussed in Section 3.2.4.

#### *3.2.2. Finless vortex tube*

Fig. 10 shows the color contours of the temperature, velocity, and pressure distributions in the cross section of the Finless. The highest velocity is simulated at the connection from the swirl generator to the hot tube. Also, the temperature of the air is the lowest in this part. After that, the air temperature increases along the hot tube. Comparing Fig. 8 (a1), which shows the surface temperature distribution measured by the IR video camera, and Fig. 10 (a), which shows the air temperature distribution simulated by the CFD code, it can be seen that both temperature distributions along the hot tube are in good agreement.

The results of the CFD analysis of Finless were consistent in trend with the results from CFD analysis reported previously [15, 24].

#### *3.2.3. Type-A Fin vortex tube*

Fig. 11 shows the color contours of the temperature, velocity, and pressure distributions in the cross section of the Type-A Fin.  In the Type-A Fin, the air temperature is higher at the position indicated by the arrow in Fig. 11 (a). Fig. 11 (b') indicates the axial velocity component. Fig. 11 (b) and (b') show that the hollow helical fin forms high velocity swirl currents towards the cold and hot exits inside the hollow, bounded by the stagnation point. Fig. 11 (c) shows that the pressure increases at the periphery side of the stagnation point, and the formation of the stagnation point results in the formation of a high-speed reversing current in the hollow of the cold end of the helical fin as shown in Fig. 11 (b').

Fig. 12 (a) and (c) show the 3D view of air streamlines colored by axial velocity component and temperature near the cold end of the fin, respectively. It can be seen from the simulation of the streamlines toward the cold exit in Fig. 12 (a) that some swirling flow of air reaches the stagnation point and its velocity decreases. From the correlation between the experimental and analytical results, the stagnation point is considered to be formed at the position "High" where the surface temperature is the highest, as shown in Fig. 8 (b1). Fig. 12 (b) shows the formation of a short and strong helical vortex flow between the cold-fin-end and the stagnation point, with a small recirculating vortex structure shown in the red and blue ellipses in Fig. 12(b).

Due to the formation of this small recirculating vortex structure, over a short axial distance, the temperature of the air toward the central axis will decrease due to adiabatic expansion, while the temperature of the air toward the peripheral direction will increase due to adiabatic compression. On the other hand, in the axial direction, the air moves toward the stagnation point where the pressure is high, so the velocity of the axial component decreases and the temperature increases due to adiabatic compression. It is thought that these adiabatic expansion and compression effects in the radial and axial directions occur in a combined manner in three dimensions. In other words, Fig. 12 (a), (b) and (c) suggest that a particularly large energy conversion from kinetic energy to internal energy takes place between the cold-fin-end and the stagnation point. As a result, the surface temperature of the hot tube increases in this area as shown in Fig. 8 (b1) and (b2).

The velocity of the reversing current formed in the hollow becomes very high at the cold-fin-end as shown in Fig. 12 (b) and Fig. 11 (b'). In the hollow, the axial velocity component of the air increases with decreasing temperature from the stagnation point where the pressure is high to the cold-fin-end where the pressure is low. The temperature is further reduced by adiabatic expansion from the narrow hollow to the wide inner space of the tube and then to the cold exit where the pressure is even lower while reducing the temperature.

### *3.2.4. Type-B Fin vortex tube*

The Type-B Fin also indicated higher cooling performance comparing with the Finless under the condition that the cold mass fraction was less than 0.4 as shown in Fig. 5.

Therefore, numerical simulations have also been conducted for the Type-B Fin.

Fig. 13 shows the 3D view of air streamlines colored by velocity or temperature in the Type-B Fin. As shown in Fig. 13 (a1), the air becomes very slow near the stagnation point, on the other hand as shown in Fig. 13 (a2), the temperature increases simultaneously and reaches a maximum at the stagnation point. This trend is the same as that of the Type-A Fin shown in Fig. 12.

Fig. 13 (b1) and (b2) show that the air flowing past the stagnation point and towards the hot exit tends to flow through the hollow and continues to flow through the hollow at high velocity. The air toward the hot exit tends to be divided into two types: flowing at high velocity in the hollow and flowing along the periphery side. The air flowing along the periphery of the fin has a lower velocity and a higher temperature than the air flowing inside the hollow.

Let us consider increasing the cold mass fraction, i.e., increasing the mass flow rate of the reverse flow to the cold exit side. In the Type-B Fin, the air flowing along the helical fin tries to flow toward the central axis. This inward flow in the forward direction and the flow backward in the hollow toward the cold exit from the stagnation point are considered to be violently colliding with each other. The reason for the decrease in energy separation performance of the Type-B Fin with a cold mass fraction $\xi$ of 0.4 or higher is considered to be that the flow rate flowing backward in the hollow increases

Similarly, the reason for the decrease in energy separation performance of Type-A Fin above the cold mass fraction $\xi$ of 0.7 as shown in Fig. 5 can be attributed to the increase in the mass flow rate of the reverse flow towards the cold exit and the change in turbulent structure with poor heat transfer.

## 4. Improvement for industrial applications

Many existing Finless VT experiments have shown that the highest energy separation performance is achieved under $L/D$ of 20 to 30. For this reason, experiments and analyses have been conducted with $L/D$ fixed at 25.1. On the other hand, when considering industrial applications, a smaller value of $L/D$ is preferable. Therefore, the author focused on the difference in stagnation point as the difference between the simulation results of Finless and Type-A Fin, and tried to improve the $L/D$ to a smaller value.

### *4.1. Experiment for the short vortex tube*

Fig. 14 illustrates a schematic drawing of the Type-A Fin test sections with $L/D$ and fin-pitch as parameters, and Fig. 15 shows the experimental results at $Gap$ = 1.5mm, $\Phi$ =

10mm and $P_{in}$ = 0.4 MPa. From the experimental results, the following were found:

1. In case of *Pitch* = 20 mm, $L/D$ = 10.0, which can provide the better energy separation performance as $L/D$ = 25.1.
2. In case of *Pitch* = 30 mm, $L/D$ = 10.0, which can provide almost the same energy separation performance as $L/D$ = 25.1.
3. There is no significant difference in energy separation performance with or without the space between the hot-fin-end and the hot plug.
4. On the other hand, the performance decreases significantly when the distance between the swirl generator and the cold-fin-end is shortened from 108 mm to 30 mm.

To summarize the experimental investigation for improvement, it is possible to produce the short VT with the high energy separation performance by adding the hollow helical fin.

It was found from the visualization of surface temperature distribution recorded by the IR still camera that the hot temperature points change significantly depending on the cold mass fraction. Fig. 16 shows the visualization results of the short VT with *Pitch* = 30 mm and $L/D$ = 10.0. The following were observed:

1. The cold-fin-end is always hot.
2. Under conditions with a low cold mass fraction, a high temperature point may also occur on the cold exit side as shown in Fig. 16 (c1).
3. The wall temperature is highest when the cold mass fraction is about 0.7. At this time, as shown in Fig. 16 (c2), the temperature is high over a wide area near the cold-fin-end.
4. When the cold mass fraction = 1, the temperature is uneven, but the overall temperature is high as shown in Fig. 16 (c3).

### *4.2. CFD analysis for the short vortex tube*

Fig. 17 indicates the computational grid and the simulation results for the short Type-A Fin VT with $L/D$ = 10.0. The following points were confirmed from the analytical results, in comparison with the results for $L/D$ = 25.1 as shown in Fig. 11 and Fig. 12.

1. Stagnation point locates inside of the hollow helical fin as well as a long Type-A Fin VT, but moves to the cold exit side.
2. Pressure is high at the stagnation point, and the velocity, temperature and pressure distribution change to a compressed form in the short section between cold exit and hot exit.

It was considered that the occurrence of turbulence affected the energy separation performance and the tube surface temperature. For this reason, parameters indicating the degree and characteristics of turbulence, such as turbulence kinetic energy, turbulence eddy dissipation, coefficient of eddy viscosity, and Reynolds stress, were visualized.

Fig. 18 (a1) and (a2) show the spatial distribution of turbulence kinetic energy, (b1) and (b2) show the spatial distribution of turbulence eddy dissipation, and (c) shows the axial component of Reynolds stress. Following were found from these turbulence analysis results:

1. Turbulence intensity is higher at the outer circumference of the inlet side and in the hollow region near the cold-fin-end.
2. The turbulent vortex dissipation velocity is higher in the outer periphery from the inlet to the stagnation point and in the hollow region near the cold-fin-end.
3. Coefficient of eddy viscosity calculated from the turbulence kinetic energy and turbulence eddy dissipation, and also Reynolds stress have large maxima in the hollow region near the cold-fin-end.
4. The axial locations of high turbulence kinetic energy and turbulent eddy dissipation coincide with the locations of high tube surface temperatures shown in Fig. 16.

These results suggest that the hollow helical fin shorten the VT by moving the stagnation point toward the inlet, and that the energy separation is enhanced by the generation of a region near the cold-fin-end where the turbulence kinetic energy, turbulence eddy dissipation, and Reynolds stress are locally higher, resulting in a higher temperature separation than in the conventional finless system.

## 5. Conclusion

The vortex tube with the hollow helical fin was developed as an air spot cooler for machining with higher temperature difference than the conventional Finless simple vortex tube. The temperature difference characteristics and surface temperature distribution were experimentally evaluated using Finless, Type-A Fin, and Type-B Fin vortex tubes. The CFD analysis was conducted to understand the flow structure inside each vortex tubes. The results and discussion of the experiments and analysis are summarized as follows:

1. The hollow helical fin fixed inside the hot tube enhances the temperature separation of the vortex tube. And the tube length can be shorten using by the fin such as from $L/D$ = 25.1 to 10.0.

When the cold mass fraction ξ was less than or equal to 0.4, the temperature difference between the inlet and cold exit of Type-A Fin was 10 °C larger than that of Finless vortex tube in the case of the $P_{in}$=0.45 MPa and ξ=0.35. In the experiment with Type-A Fin, the minimum air discharge temperature was -45 °C and the maximum temperature difference between inlet and cold exit $\Delta T_c$ was 62.2 °C.

2. The stagnation point has a significant effect on the flow structure and temperature distribution of the vortex tube.

   When the cold mass fraction is 0.2, the stagnation point of the Finless vortex tube is located at the hot exit side. The length of the reversing current of the air discharged from the cold exit is longer, and the surface temperature is higher at the hot exit side where the stagnation point is located. On the other hand, if there is the hollow helical fin, the stagnation point is near the cold-fin-end, the length of the reversing current of air discharged from the cold exit is short. The air temperature and also the surface temperature of the hot tube reach their maximum values at the stagnation point.

3. The reason why the hollow helical fin enhances cooling performance is that a short and strong reversing helical vortex flow between the cold-fin-end and the stagnation point is formed with a small recirculating vortex structure. In this region, turbulence kinetic energy, turbulent eddy dissipation, and Reynolds stress are also high.

   The formation of the high turbulence kinetic energy region may cause high heat transfer in the radial direction. As a result, the surface temperature of the hot tube increases in this area. After lowering the temperature by increasing the axial velocity component from the stagnation point to the cold-fin-end, the temperature is further lowered by adiabatic expansion from the narrow hollow to the wide space inside the circular tube and then to the cold exit where the pressure is even lower while reducing the temperature.

   The high turbulent kinetic energy region generated by the hollow inclined helical fin improves the cooling performance of the vortex tube.

## Author statement

M. Kureta; conducted the research, wrote the paper, designed the new vortex tubes
Y. Yamagata; managed the experimental research and team
K. Miyakoshi; welded the vortex tubes, collected the data
T. Mashii; made the vortex tubes, collected the data
Y. Miura; built the measurement and data processing system, collected the data
K. Takahashi; modeled and simulated by the CFD code
All authors had approved the final version.

## Declaration of competing interest

There is no conflict of interest for this manuscript.

## Acknowledgment

Part of this work was supported by Tokai-mura [Innovation Creation Project 2020: No.846]. The VT with a hollow helical fin has been applied for a patent (Japanese patent application No. 2021-122954 and No. 2022-096172).

All CFD simulations were performed using a workstation at the Industrial Technology Innovation Center of Ibaraki Prefecture. The authors also acknowledge the support from President Eisaku Sato and Mr. Masao Yoshida of ART KAGAKU Co. Ltd. We are especially grateful for the assistance provided by Ms. Akemi Sagawa of JAEA in filing the patent application.

The infrared cameras used in this report were borrowed from Dr. Shinichiro Uesawa and Dr. Takuya Nankawa. Thank you for their support.

## References

[1] H. Takahama, Studies on vortex tubes (1) Experiments on efficiency of energy separation (2) On profiles of velocity and temperature, Bulletin of JSME, 8(31) (1965) 433-440.

[2] K. Stephan, S. Lin, M. Durst, F. Huang, D. Seher, An investigation of energy separation in a vortex tube, International Journal of Heat and Mass Transfer, 26 (3) (1983) 341-348.

[3] K. Stephan, S. Lin, M. Durst, F. Huang, D. Seher, A similarity relation for energy separation in a vortex tube, International Journal of Heat and Mass Transfer, 27 (6) (1984) 911-920.

[4] G. J. Ranque, Method and apparatus for obtaining from a fluid under pressure two

currents of fluid at different temperatures, US Patent 1952281 (1934).
[5] R. Hilsch, The use of the expansion of gases in a centrifugal field as cooling process, Review of Scientific Instruments, 18(2) (1947) 108-113.
[6] C. Gao, Experimental study on the Ranque-Hilsch vortex tube, Technische Universiteit Eindhoven (2005) ISBN 90-386-2361-5.
[7] R. Liew, J. C. H. Zeegers, J. G. M. Kuerten, W. R. Michalek, Maxwell's Demon in the Ranque-Hilsch vortex tube, Physical Review Letters, 109 (5) 054503 (2012).
[8] R. Liew, Droplet behaviour and thermal separation in Ranque-Hilsch vortex tubes, Technische Universiteit Eindhoven (2013).
[9] Y. Xue, M. Arjomandi, R. Kelso, Experimental study of the flow structure in a counter flow Ranque-Hilsch vortex tube, International Journal of Heat and Mass Transfer, 55 (21-22) (2012) 5853-5860.
[10] Y. Xue, The working principle of a Ranque-Hilsch vortex tube, The University of Adelaide (2012) 139p.
[11] S. E. Rafiee, M. M. Sadeghiazad, Experimental study and 3D CFD analysis on the optimization of throttle angle for a convergent vortex tube, Journal of Marine Science and Application, 15 (2016) 388-404.
[12] L. M. K. Zangana, R. R. I. Barwari, The effect of convergent-divergent tube on the cooling capacity of vortex tube: An experimental and numerical study, Alexandria Engineering Journal, 59 (2020) 239-246.
[13] H. Kaya, O. Uluer, E. Kocaoglu, V. Kirmaci, Experimental analysis of cooling and heating performance of serial and parallel connected counter-flow Ranque-Hilsch vortex tube systems using carbon dioxide as a working fluid, International Journal of Refrigeration, 106, (2019) 297-307.
[14] D. Majidi, H. Alighardashi, F. Farhadi, Best vortex tube cascade for highest thermal separation, International Journal of Refrigeration, 85, (2018) 282-291.
[15] W. Naksanee, R. Prommas, An experimental investigation on the efficiency snail entry in vortex tube fed low inlet air pressure to reduce temperature of low pressure air, International Journal of Heat and Technology, 36 (4) (2018) 1223-1232.
[16] O. V. Vitovsky, Experimental study of energy separation in a Ranque-Hilsch tube with a screw vortex generator, International Journal of Refrigeration, 126, (2021) 272-279.
[17] M. O. Hamdan, B. Alsayyed, E. Elnajjar, Nozzle parameters affecting vortex tube energy separation performance, Heat and Mass Transfer, 49 (2013) 533-541.
[18] K. Devade, A. Pise, Effect of cold orifice diameter and geometry of hot end valves on performance of converging type Ranque Hilsch vortex tube, Energy Procedia, 54 (2014) 642-653.
[19] P. Samruaisin, V. Chuwattanakul, M. Pimsarn, P. Promthaisong, A. Saysroy, S. Chokphoemphun, M. Kumar, S. Eiamsa-ard, Influence of a double vortex chamber on

temperature reduction in a counter-flow vortex tube, Case Studies in Thermal Engineering, 28 (2021) 101662.

[20] N. I. Yavorsky, V. G. Meledin, I. K. Kabardin, M. R. Gordienko, M. Kh. Pravdina, D. V. Kulikov, V. I. Polyakova, V. A. Pavlov, Velocity field diagnostics inside the Ranque-Hilsch vortex tube with square cross-section, International Conference on the Methods of Aerophysical Research (ICMAR 2018), AIP Conference Proceedings, 2027, (2018) 030122.

[21] S. Eiamsa-ard, P. Promvonge, Numerical investigation of the thermal separation in a Ranque-Hilsch vortex tube, International Journal of Heat and Mass Transfer, 50 (5-6) (2007) 821-832.

[22] A. Secchiaroli, R. Ricci, S. Montelpare, V. D'Alessandro, Numerical simulation of turbulent flow in a Ranque-Hilsch vortex tube, International Journal of Heat and Mass Transfer, 52 (23-24) (2009) 5496-5511.

[23] M. Baghdad, A. Ouadha, O. Imine, Y. Addad, Numerical study of energy separation in a vortex tube with different RANS models, International Journal of Thermal Science, 50, (12) (2011) 2377-2385.

[24] A. Moraveji, D. Toghraie, Computational fluid dynamics simulation of heat transfer and fluid flow characteristics in a vortex tube by considering the various parameters, International Journal of Heat and Mass Transfer, 113 (2017) 432-443.

[25] T. Farouk, B. Farouk, Large eddy simulations of the flow field and temperature separation in the Ranque-Hilsch vortex tube, International Journal of Heat and Mass Transfer, 50 (23-24) (2007) 4724-4735.

[26] T. Farouk, B. Farouk, A. Gutsol, Simulation of gas species and temperature separation in the counter-flow Ranque-Hilsch vortex tube using the large eddy simulation technique, International Journal of Heat and Mass Transfer, 52 (13-14) (2009) 3320-3333.

[27] B. Zhang, X. Guo, Z. Yang, Analysis on the fluid flow in vortex tube with vortex periodical oscillation characteristics, International Journal of Heat and Mass Transfer, 103 (2016) 1166-1175.

[28] X. Guo, B. Zhang, Analysis of the unsteady heat and mass transfer processes in a Ranque-Hilsch vortex tube: Tube optimization criteria, International Journal of Heat and Mass Transfer, 127 (2018) 68-79.

## Nomenclature

| | |
|---|---|
| $D$ | inner diameter of the vortex tube, mm |
| $F$ | mass flow rate, kg/h |
| $Gap$ | nozzle gap, mm |
| $L$ | inner length of the vortex tube, mm |
| $P$ | pressure, MPa |
| $Pitch$ | fin pitch, mm |
| $T$ | temperature, °C |

*Greek Symbols*

| | |
|---|---|
| $\Delta T$ | temperature difference, °C |
| $\Phi$ | diameter which is the boundary between the hollow and fin sections, mm |
| $\xi$ | cold mass fraction |

*Subscripts*

| | |
|---|---|
| $c$ | cold exit side |
| $fin$ | hollow helical fin |
| $h$ | hot exit side |
| $in$ | inlet |
| $w$ | wall, surface of the hot tube |

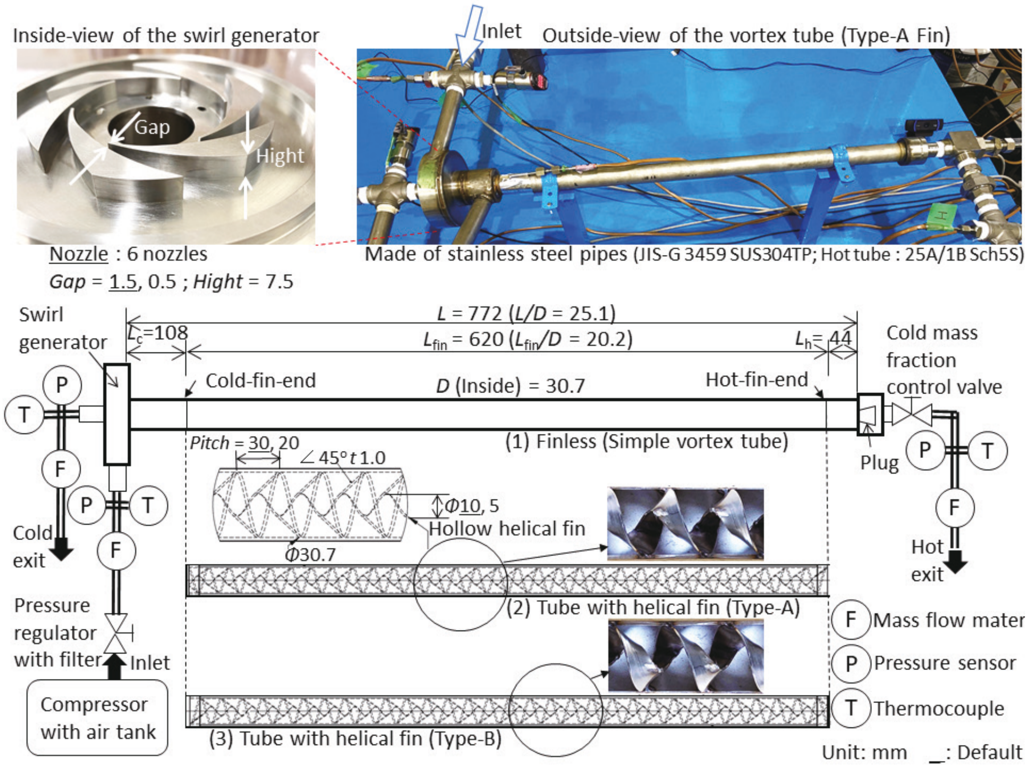


**Fig. 1.** Schematic diagram and photographs of the experimental setup.

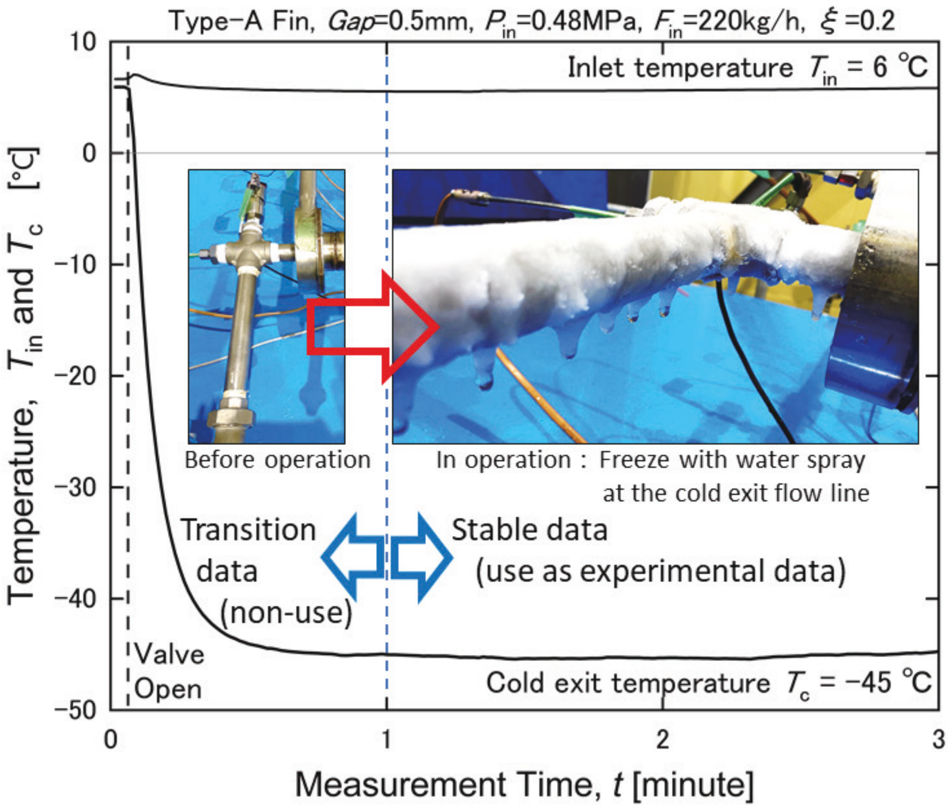


**Fig. 2.** Time variation of temperature at startup.
(The cold mass fraction control valve was fully opened.)

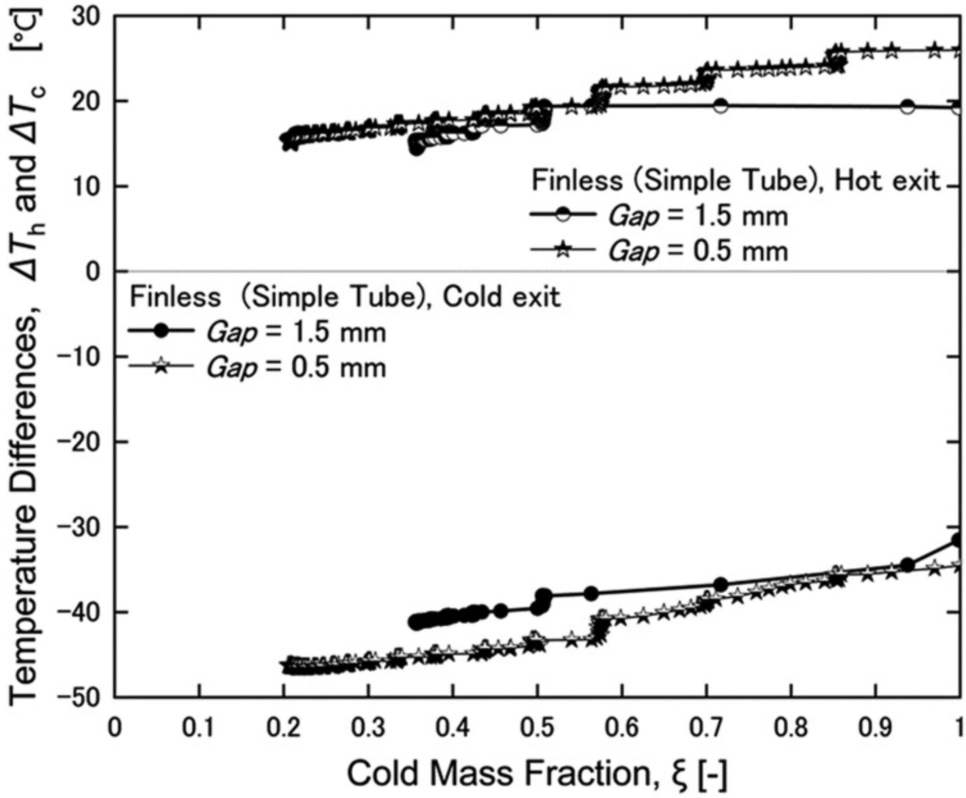


**Fig.3.** Effect of the nozzle gap in the swirl generator on the temperature differences. (Finless, $P_{\mathrm{in}}$=0.45 MPa)

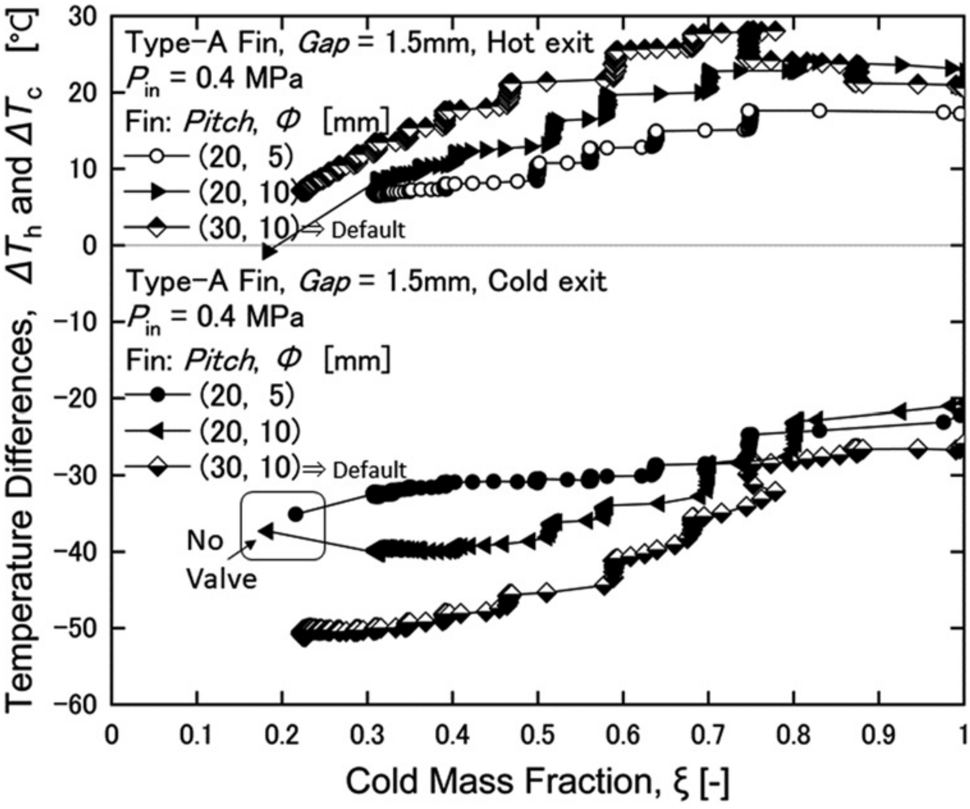


**Fig. 4.** Effect of the pitch and inner diameter of the hollow helical fin on temperature differences. (*Gap* = 1.5 mm, $P_{\mathrm{in}}$ = 0.4 MPa)

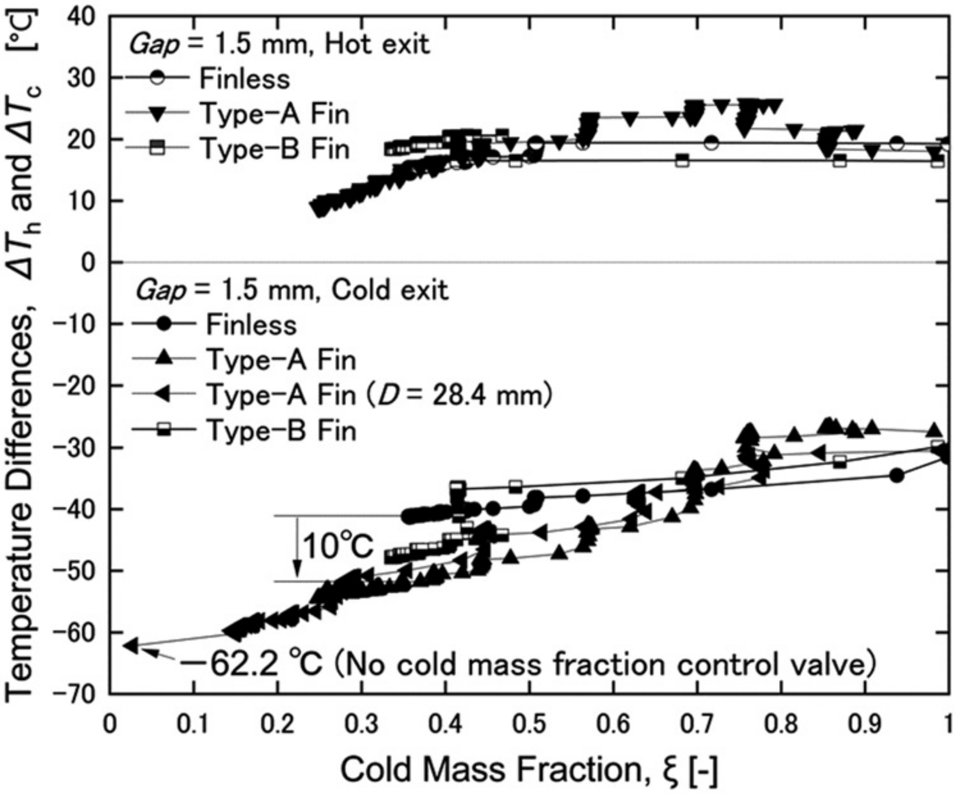


**Fig. 5.** Effect of a hollow helical fin on temperature differences.
($Gap$ = 1.5 mm, $P_{in}$ = 0.45 MPa)

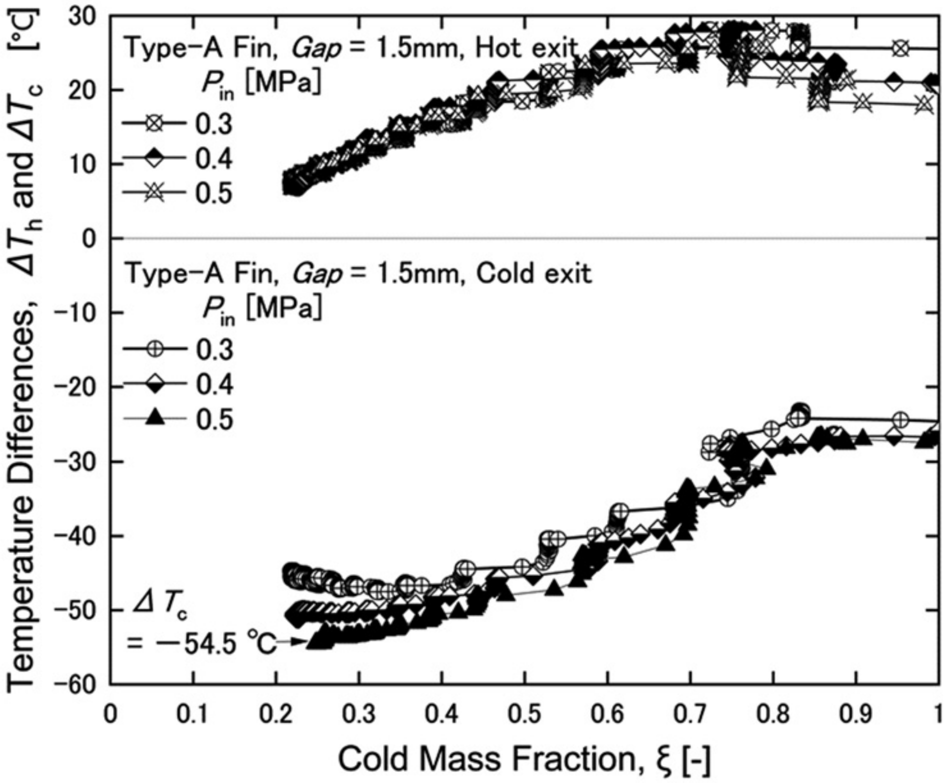


**Fig. 6.** Effect of inlet pressure on temperature differences.
(Type-A Fin, $Gap$ = 1.5 mm).

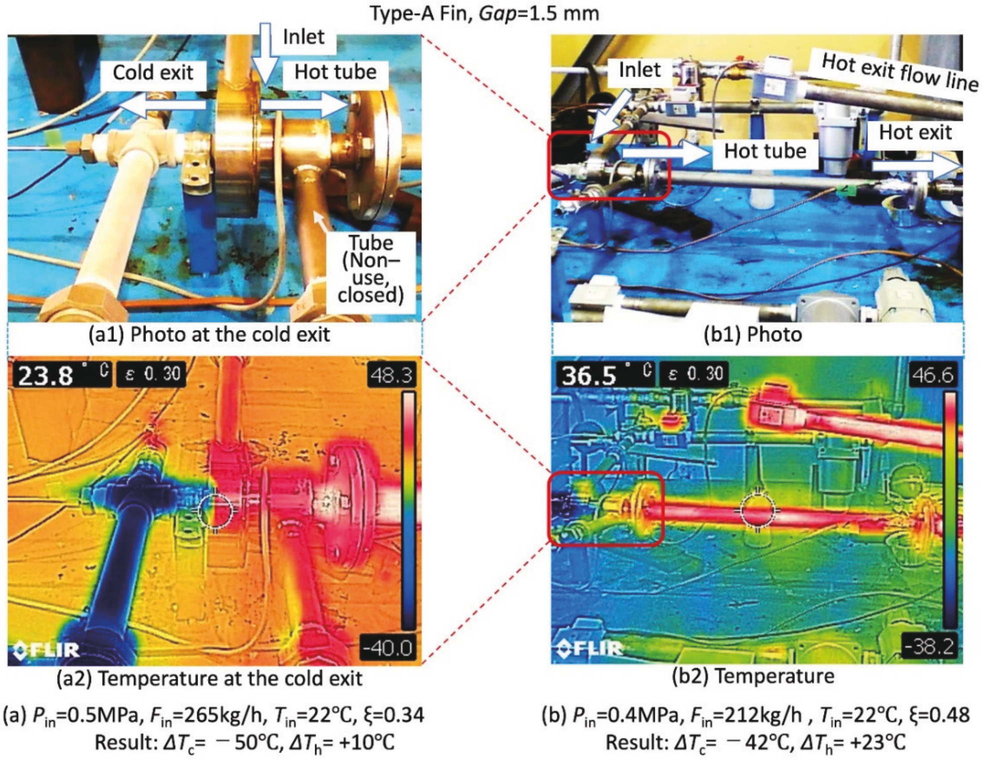


**Fig. 7.** Surface temperature distribution recorded by the IR still camera. (Type-A Fin, *Gap* = 1.5 mm).

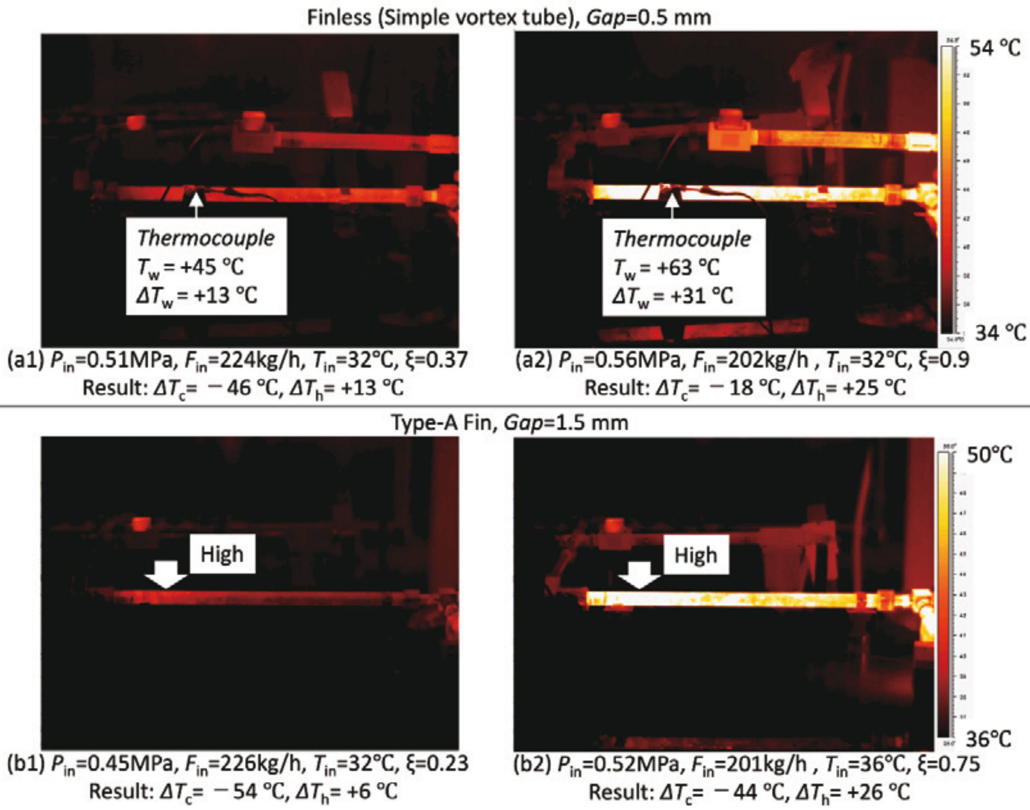


**Fig. 8.** Effect of cold mass fraction on the surface temperature distributions. ((a) Finless, *Gap* = 0.5 mm, (b) Type A Fin, *Gap* = 1.5 mm)

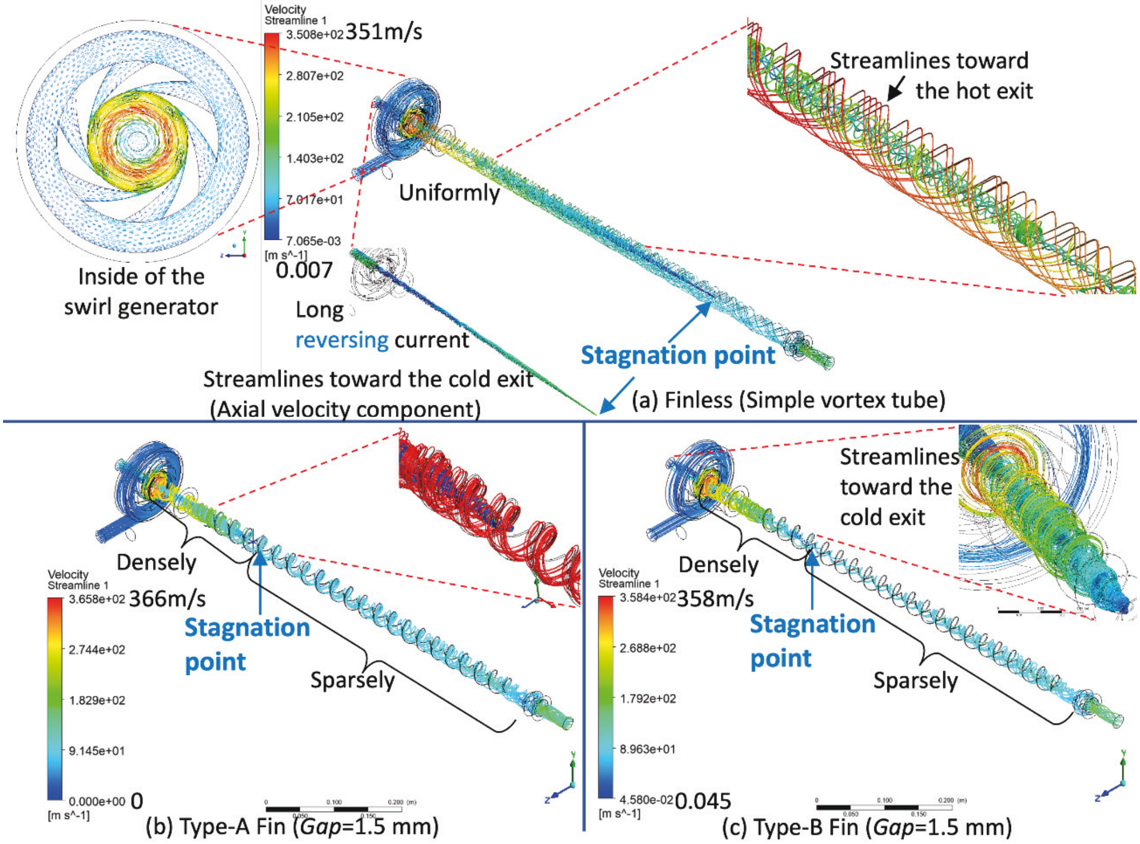


Fig. 9. Effect of the hollow helical fin on air streamlines.
((a) Finless, (b) Type-A Fin, (c) Type-B Fin)

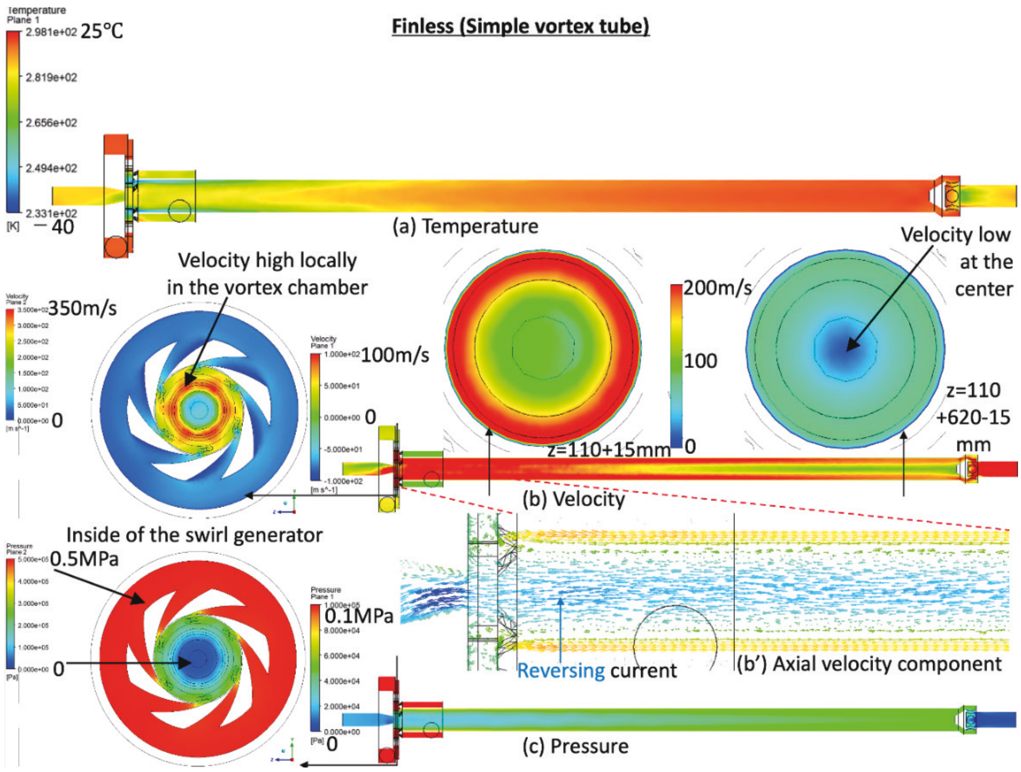


Fig. 10. Temperature, velocity and pressure distribution in the Finless vortex tube.
($P_{in}$=0.5 MPa, $T_{in}$=22 °C, ξ= 0.2)

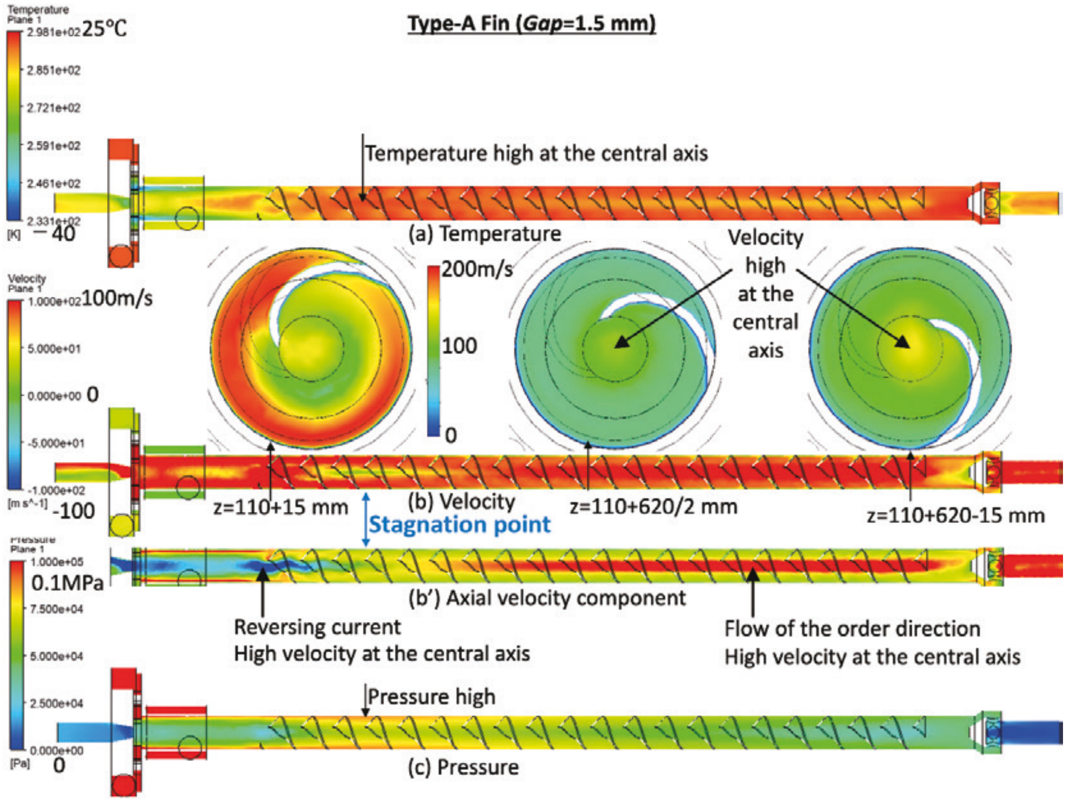


**Fig. 11.** Temperature, velocity, and pressure distributions in the Type-A Fin vortex tube.
($P_{in}$=0.5 MPa, $T_{in}$=22 °C, ξ= 0.2)

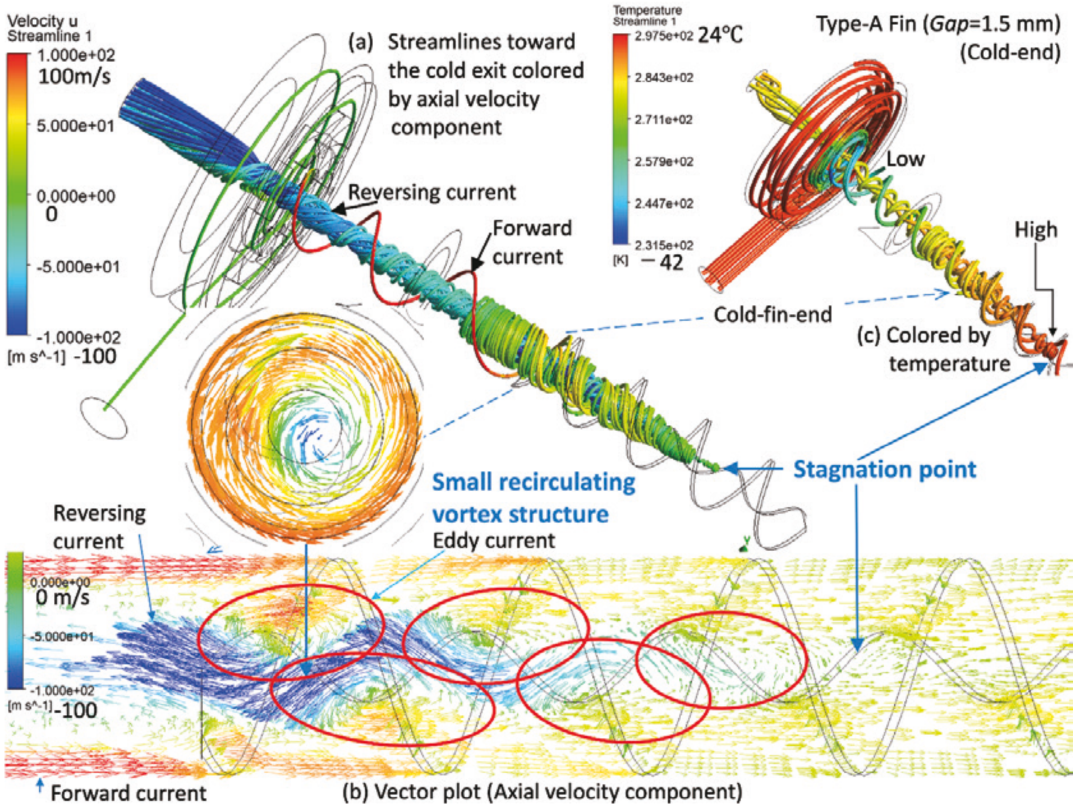


**Fig. 12.** Effect of the hollow helical fin on the flow structure at the cold end of the fin.
($P_{in}$=0.5 MPa, $T_{in}$=22 °C, ξ= 0.2)

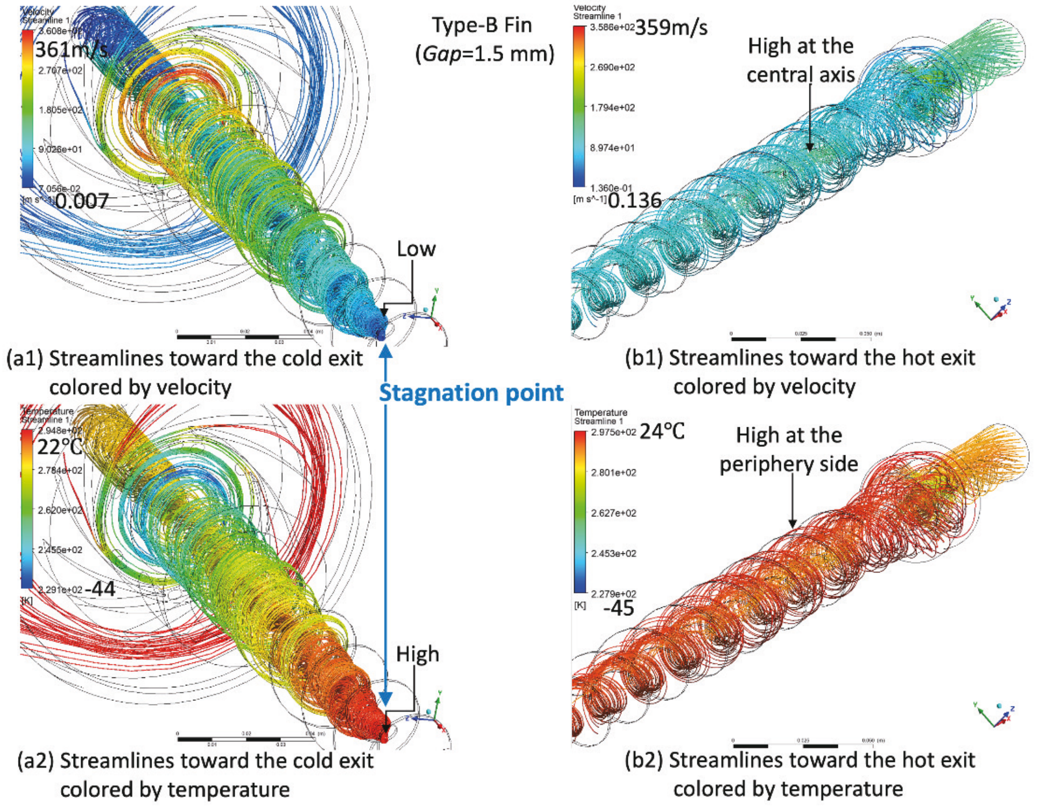


**Fig. 13.** Correlation between velocity and temperature distributions in the Type-B Fin vortex tube. ($P_{in}$=0.5 MPa, $T_{in}$=22 °C, ξ= 0.2)

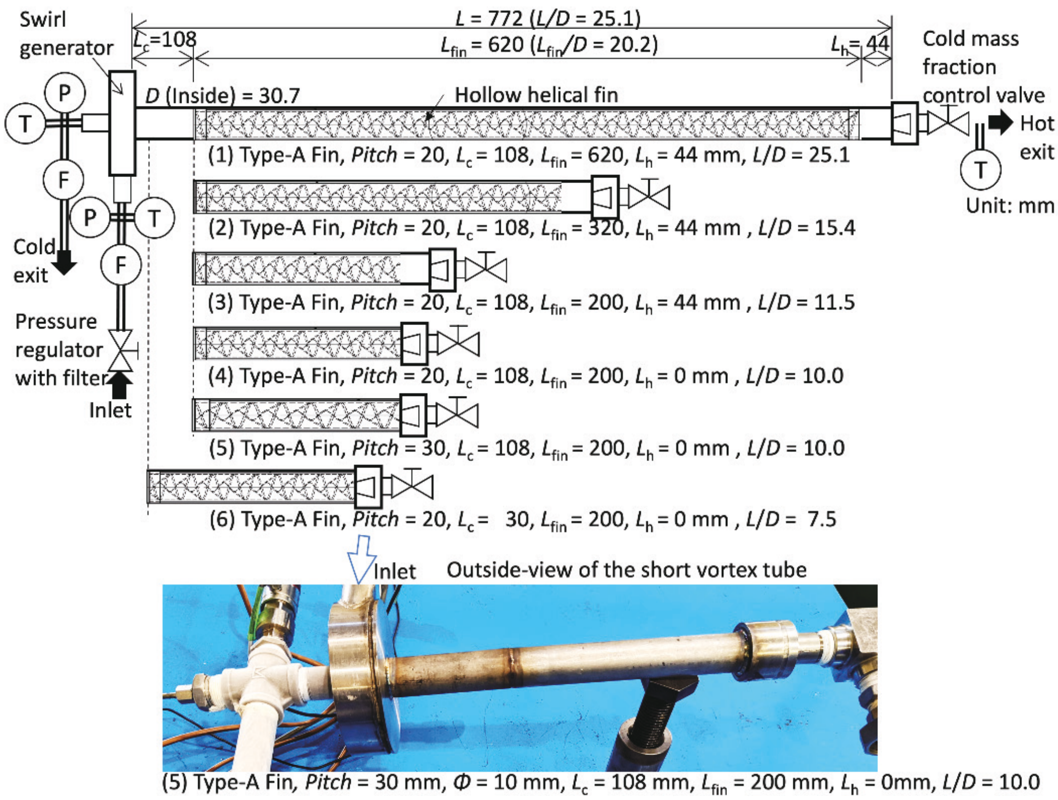


**Fig. 14.** Schematic view of the test sections for small $L/D$ experiments. (Type-A Fin vortex tube, $Gap$ = 1.5mm)

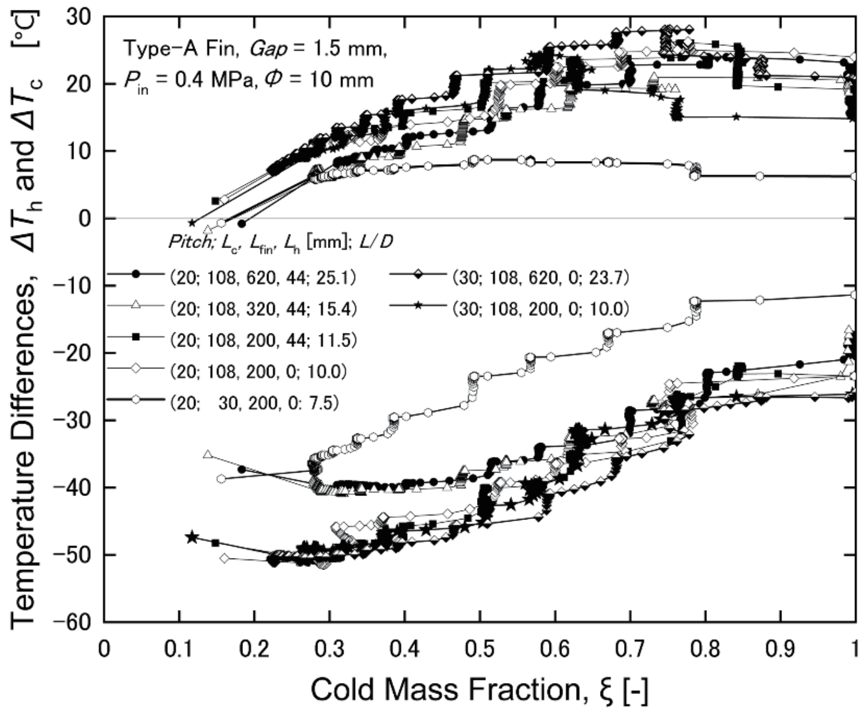


**Fig. 15.** Effect of $L/D$ and fin-pitch on temperature differences.
(Type-A Fin, *Gap* = 1.5 mm, $\Phi$ = 10mm, $P_{in}$ = 0.4 MPa)

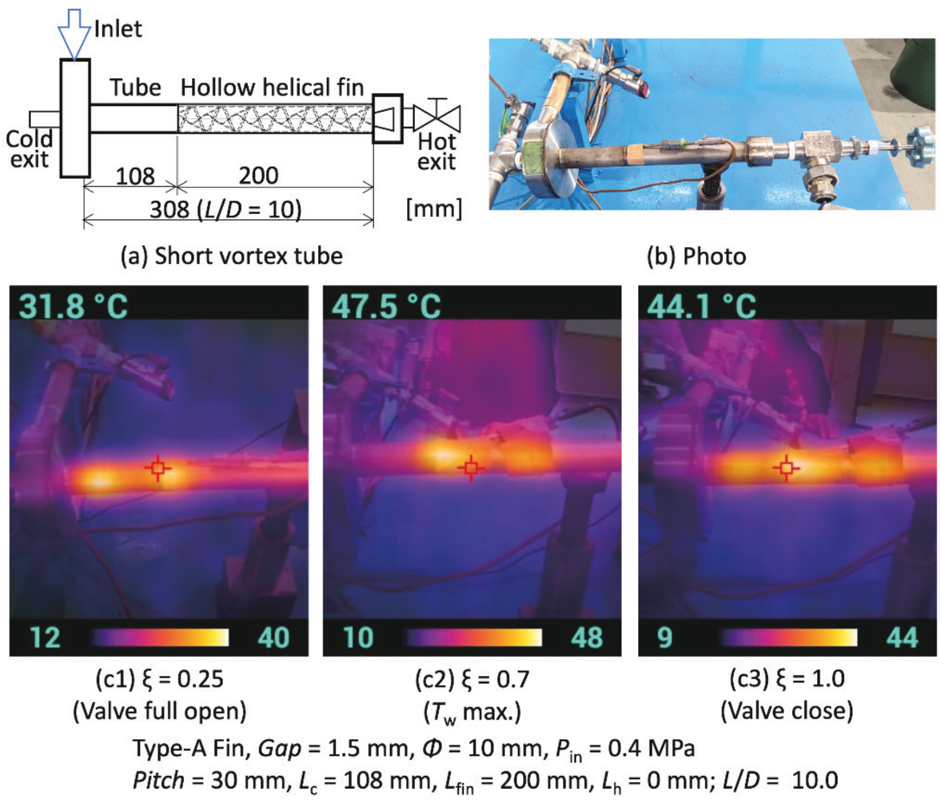


**Fig. 16.** Surface temperature distribution of the short vortex tube.

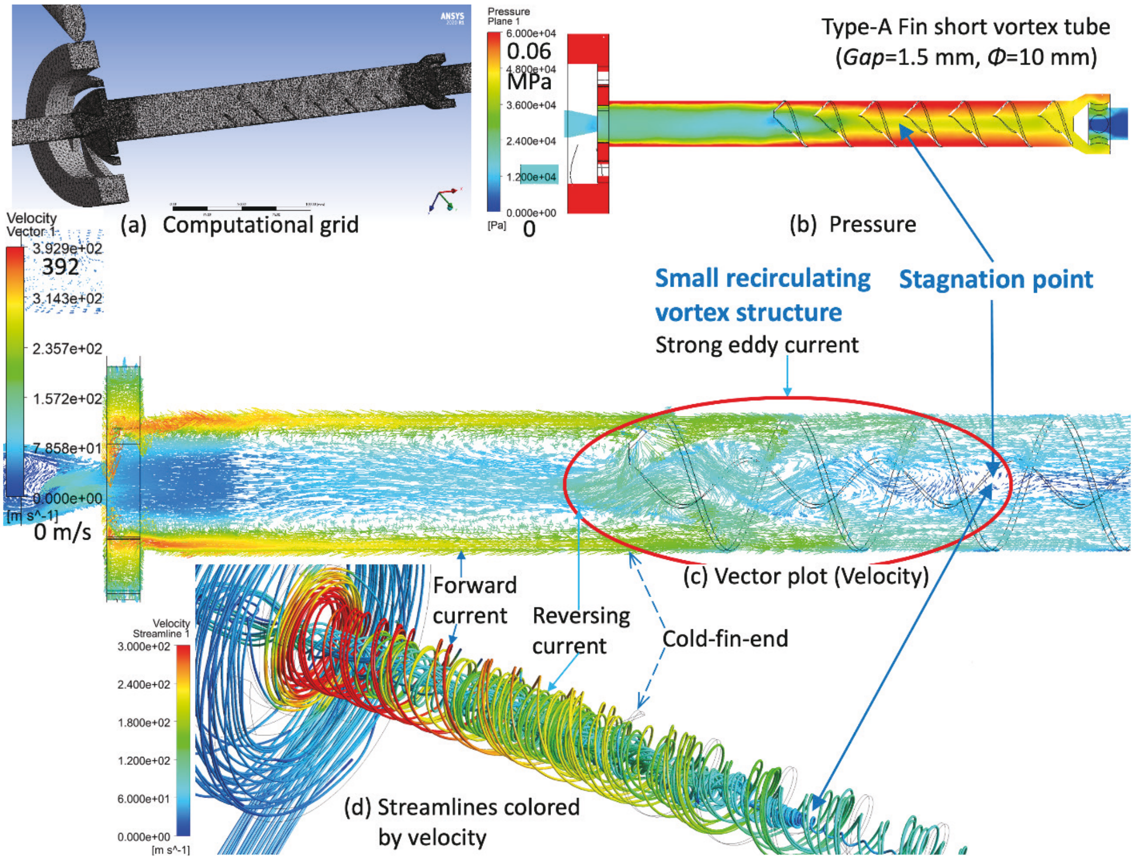


Fig. 17. The flow characteristics in the short vortex tube simulated by the CFD analysis code. ($P_{in}$=0.4 MPa, $T_{in}$ = 22.6 °C, ξ= 0.16)

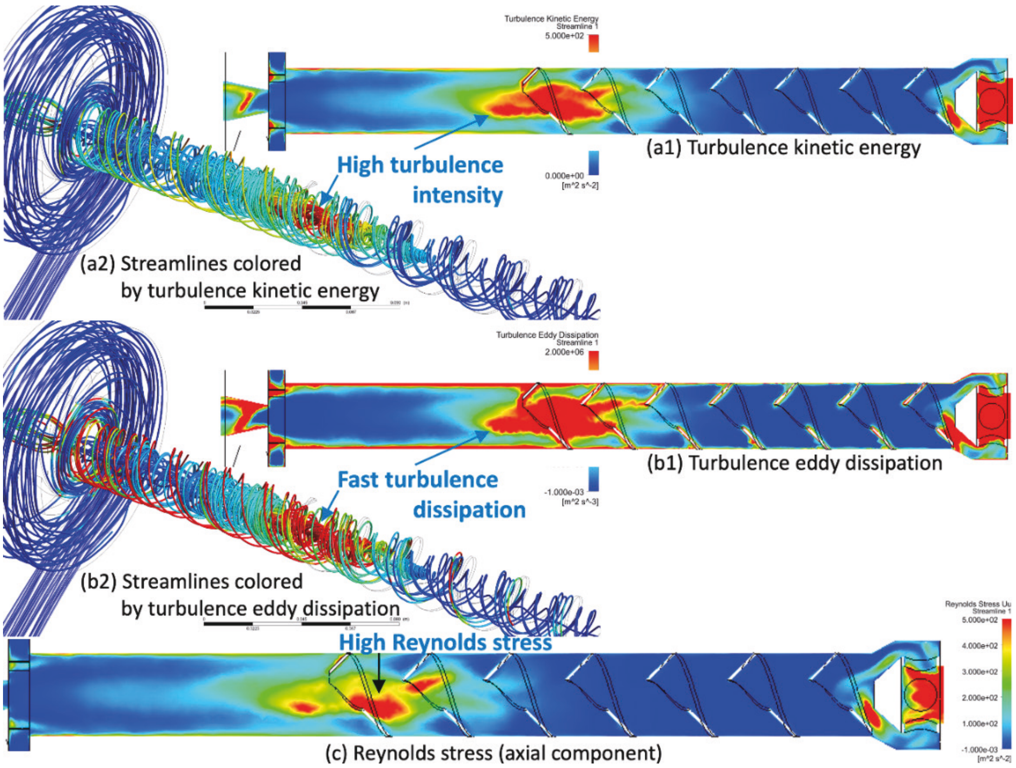


Fig. 18. The turbulence characteristics in the short vortex tube simulated by the CFD analysis code. ($P_{in}$=0.4 MPa, $T_{in}$ = 22.6 °C, ξ= 0.16)

# Appendix

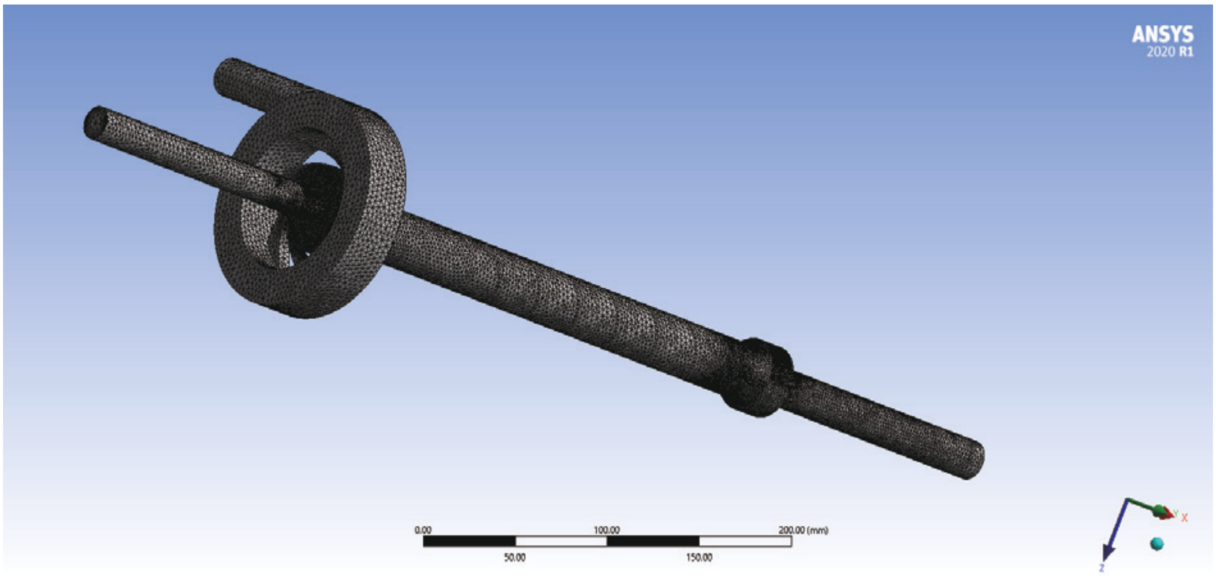


**Appendix 1.** Three-dimensional model of vortex tube
(Exterior)

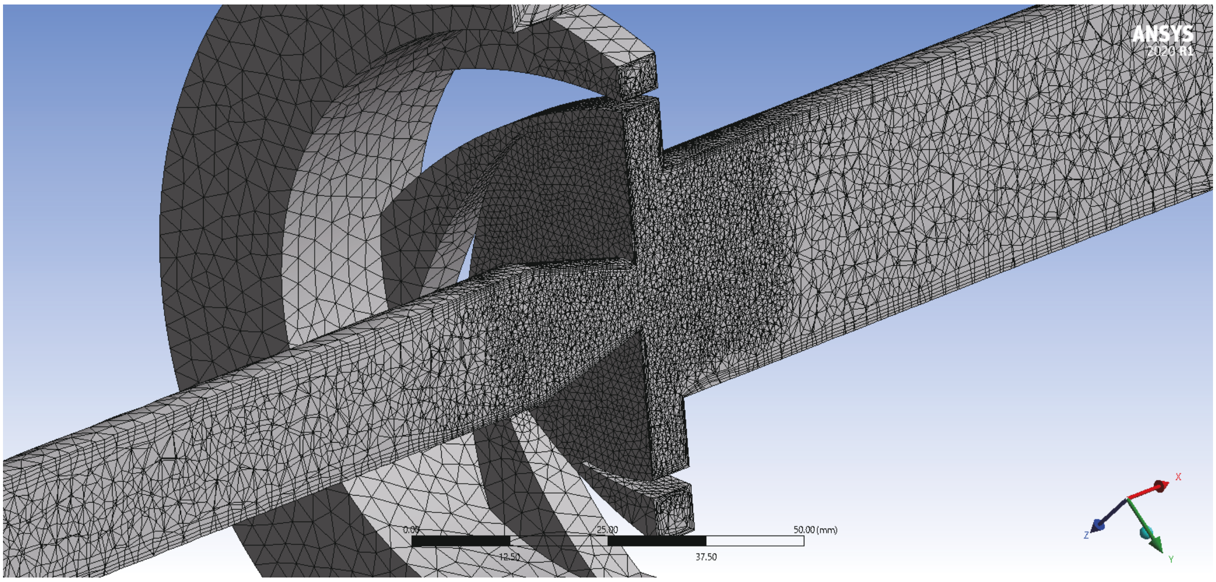


**Appendix 2.** Three-dimensional model of vortex tube
(Near the inlet and cold exit)

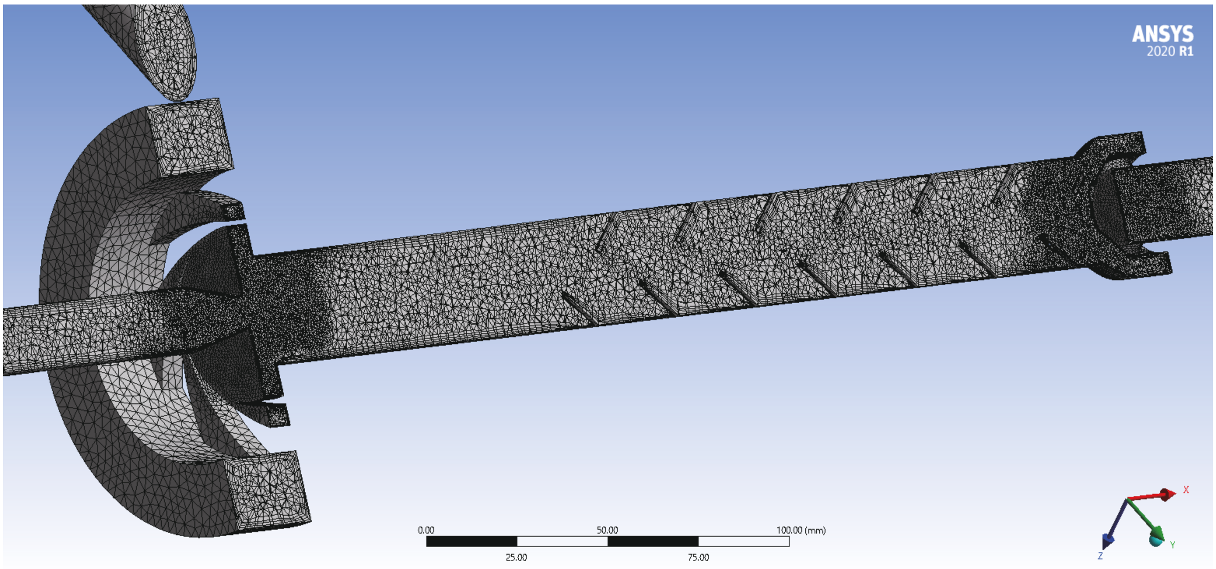


**Appendix 3.** Three-dimensional model of vortex tube
(Cross section)

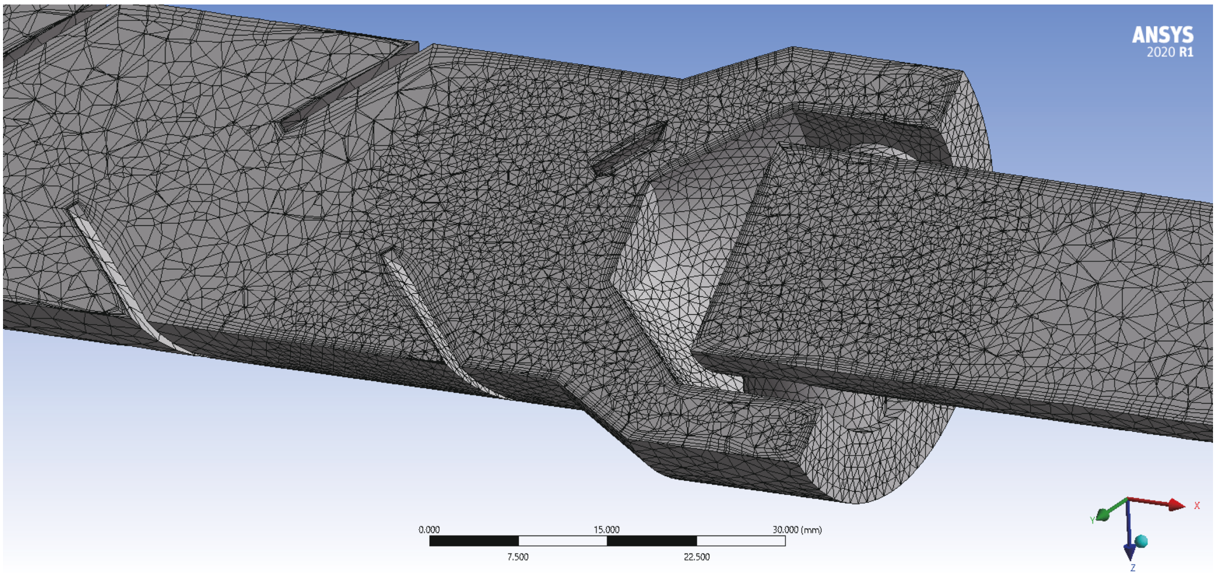


**Appendix 4.** Three-dimensional model of vortex tube
(Near the hot exit)

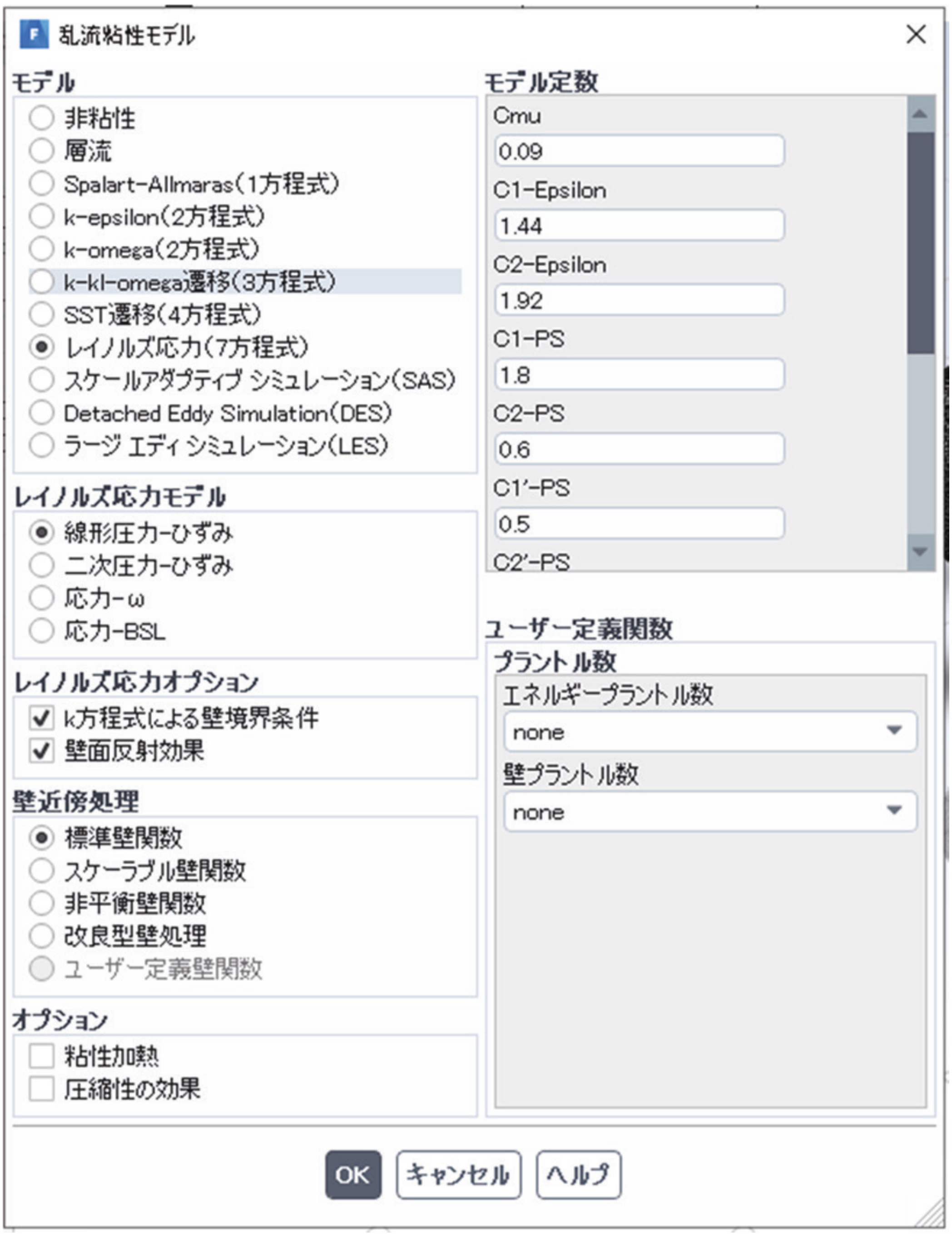


**Appendix 5.** Selected turbulent viscosity model in FLUENT analysis code (RSM, Linear pressure-strain model, Standard wall function)